PHYSICAL REVIEW B

CONDENSED MATTER

THIRD SERIES, VOLUME 55, NUMBER 6 1 FEBRUARY 1997-II

RAPID COMMUNICATIONS

Rapid Communications are intended for the accelerated publication of important new results and are therefore given priority treatment both in the editorial office and in production. A Rapid Communication in **Physical Review B** *may be no longer than four printed pages and must be accompanied by an abstract. Page proofs are sent to authors.*

X-ray fluorescence holography and multiple-energy x-ray holography: A critical comparison of atomic images

P. M. Len
Physics Department, University of California, Davis, California 95616

T. Gog
Oak Ridge National Laboratory at the National Synchrotron Light Source, Brookhaven National Laboratory, Upton, New York 11973

C. S. Fadley
Physics Department, University of California, Davis, California 95616
and Materials Sciences Division, Lawrence Berkeley National Laboratory, Berkeley, California 94720

G. Materlik
Hamberger Synchrotronstrahlungslabor HASYLAB am Deutsches Elektronen-Synchrotron DESY, D-22603 Hamburg, Germany
(Received 26 July 1996; revised manuscript received 10 October 1996)

We compare x-ray fluorescence holography (XFH) and multiple-energy x-ray holography (MEXH), two techniques that have recently been used to obtain experimental three-dimensional atomic images. For single-energy holograms, these methods are equivalent by virtue of the optical reciprocity theorem. However, XFH can only record holographic information at the characteristic fluorescence energies of the emitting species, while MEXH can record holographic information at any energy above the fluorescent edge of the emitter, thus enabling the suppression of real-twin overlaps and other aberrations and artifacts in atomic images. [S0163-1829(97)51006-X]

I. Introduction. Nearly a half century ago, Gabor proposed a holographic solution to the classic phase problem in crystal diffraction.[1] Whereas only the intensity of the wave fronts scattered by atoms in a crystal are measured in a conventional diffraction experiment, Gabor suggested that the phases of these diffracted wave fronts could be referenced to a coherent source that simultaneously illuminates the detector as well as the crystal. This technique has successfully imaged nanometer-scale structures with electrons from field-emission tips,[2] but these sources lack the necessary source size and wavelength resolution to image atomic structure on the angstrom scale. However, Szöke noted about a decade ago that photoexcited atoms within the sample itself may serve as highly coherent sources of outgoing electron or fluorescent x-ray waves.[3] This ''inner-source'' implementation of Gabor's holographic solution to the phase problem has by now enabled three-dimensional atomic images with subangstrom resolution to be directly obtained from photoelectron diffraction, for example.[4–17] However, it is also well recognized that electron scattering is highly nonideal, with angular anisotropies in scattering amplitude and phase that can distort images, and multiple scattering effects that can complicate analysis. Since x rays scatter much more ideally than electrons, inner-source x-ray holography represents a potentially promising approach as well.[18,19]

Two experimental approaches have recently obtained holographic atomic images using x rays: x-ray fluorescence holography[18–20] (XFH) and multiple-energy x-ray holography (MEXH).[21,22] For a given single energy, holographic measurements made by these methods are equivalent by virtue of the optical reciprocity theorem, and will result in equally resolved atomic images. However, MEXH is capable of recording holographic intensities at arbitrary energies, which can suppress twin image effects, as well as other ab-

errations and artifacts in reconstructed images, as we illustrate below in theoretical simulations for several imaging strategies.

II. Optical reciprocity of MEXH and XFH. We first discuss the creation of holographic diffraction patterns from atomic scattering, in Gabor's original scheme, as shown in Fig. 1(a).[1] Here, a convergent beam is brought to a point focus near an atom, where it begins to diverge as it illuminates both the nearby atom and a far-field screen. The wave front scattered by the atom will reach a given position on the screen and interfere with the direct, unscattered wave front. The intensity pattern will depend on the phase difference between the scattered and unscattered wave fronts, *which for ideal pointlike scattering* is solely due to the difference between their path lengths (l and l_0, respectively). Thus the phase of the scattered wave front is visible in the holographic diffraction pattern $I(\mathbf{k})$ on this screen, as it is referenced at each point to the direct wave front.

In the simplest implementation of XFH as first suggested by Szöke,[3] the point focus of the coherent beam is replaced by an (ideally pointlike) atom that is photoexcited to emit a spherical fluorescent x-ray wave front [Fig. 1(b)]. Similar to Gabor's original scheme, the wave fronts scattered by atoms neighboring the emitter will reach a far-field detector, where they will interfere with the direct, unscattered portion of the emitted wave front. Moving the detector over a large solid-angle range will then generate a holographic interference pattern $I(\mathbf{k})$ over different emission directions $\mathbf{k}$, due to the changing differences in the path lengths between the scattered and direct wave fronts.

MEXH can be thought of as a time-reversal implementation of XFH,[21,22] in which the directions of all the paths in the XFH case are reversed, together with the locations of the wave source and detector [Fig. 1(c)]. A far-field point source illuminates the sample with x rays having an energy higher than a particular absorption edge of a specific emitter of interest. This emitter will then be excited by a wave field that is a superposition of wave fronts scattered by neighboring atoms, and the direct, unscattered wave front. The interference between the scattered and direct wave fronts at the location of the fluorescing atom depends solely on the difference between their path lengths, as traced back to the far-field source, and the resulting wave field strength at the emitter determines the amount of fluorescence generated. Now moving the *source* relative to the sample over a large range of solid angle with the detector fixed in direction and averaging over a large solid angle enables recording a holographic intensity pattern $I(\mathbf{k})$ over different directions, again due to the changing difference in path lengths between the scattered and direct wave fronts.

Note that we have assumed the presence of only one fluorescing atom, whether it acts as the coherent wave source, or the path length difference detector. Realistically there will be many fluorescing atomic sites, but if each photoemitter has an identical neighborhood, then this presents no problem, as the reconstructed atomic images will merely be the superposition of each identical neighborhood.[3] If there exist a small number of inequivalent emitter sites, then the reconstructed image intensities will be a superposition of the neighboring environments surrounding each emitter.[22]

For all three experimental schemes, the phases of the scattered wave fronts are referenced to the differences in path length that they have relative to the direct unscattered wave $I_0(\mathbf{k})$. If the jth scatterer is at position $\mathbf{a}$, relative to the emitter, then these path length differences generate a phase of $\mathbf{k}\cdot\mathbf{a}_j - ka_j$, which over $\mathbf{k}$ space are unique for each $\mathbf{a}_j$ scatterer. Thus, a sufficient data set throughout $\mathbf{k}$ space and involving the resulting phase factor $e^{i(\mathbf{k}\cdot\mathbf{a}_j - ka_j)}$ will uniquely identify each scatterer at relative positions $\mathbf{r}=\mathbf{a}_j$ from the point focus or emitter. Holographic intensities $\chi(\mathbf{k})$ are now generated by subtracting and then dividing out the unscattered wave $I_0(\mathbf{k})$ from the measured holographic intensities $I(\mathbf{k})$, and these will be given by

$$\chi(\mathbf{k}) = [I(\mathbf{k}) - I_0(\mathbf{k})]/I_0(\mathbf{k}) . \tag{1}$$

In a simple single scattering model of the scattering process, we can also write[3]

$$\chi(\mathbf{k}) \propto \sum_j [f(\Theta^{\mathbf{k}}_{\mathbf{a}_j})/ka_j]\, e^{i(\mathbf{k}\cdot\mathbf{a}_j - ka_j)} + \text{c.c.}, \tag{2}$$

where $f(\Theta^{\mathbf{k}}_{\mathbf{a}_j}) \equiv |f(\Theta^{\mathbf{k}}_{\mathbf{a}_j})| e^{i\psi(\Theta^{\mathbf{k}}_{\mathbf{a}_j})}$ is the atomic scattering factor, and $\Theta^{\mathbf{k}}_{\mathbf{a}_j}$ is the angle between $\mathbf{k}$ and $\mathbf{a}_j$. Inverting such a hologram at a single energy via

$$U(\mathbf{r}) = \int\int_{\Omega} d\sigma_{\mathbf{k}} e^{-i\mathbf{k}\cdot\mathbf{r}} \chi(\mathbf{k}) \tag{3}$$

shows that the first term in $\chi(\mathbf{k})$ will reconstruct holographic real images at $\mathbf{r}=\mathbf{a}_j$, while the complex conjugate term will result in holographic twin images at $\mathbf{r}=-\mathbf{a}_j$. Extending Eq. (3) so as to simultaneously invert images at multiple energies produces intensity peaks only at the real locations of the

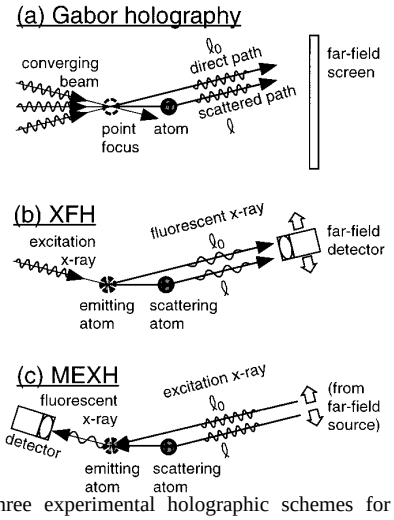

FIG. 1. Three experimental holographic schemes for recording the phases of atomically scattered wave fronts by referencing them to a direct, unscattered wave front. (a) Gabor's original proposal, where an external coherent beam is brought to a point focus near the scattering atoms, and the resulting scattered and unscattered wave fronts are collected on a far-field screen. (b) X-ray-fluorescence holography (XFH). The point focus of the coherent beam in (a) is replaced by a fluorescing atom, while a far-field detector is moved in order to collect the scattered and unscattered wave fronts over a range of different directions. (c) Multiple-energy x-ray holography (MEXH). The time-reversed version of XFH, in which a far-field coherent plane-wave source is moved over a range of different directions, while the fluorescing atom senses the superposition of the scattered and unscattered wave fronts, and a remote *stationary* detector collects the amount of fluorescence from the emitter. The incident waves in MEXh can be of any energy above the absorption edge of the emitter.

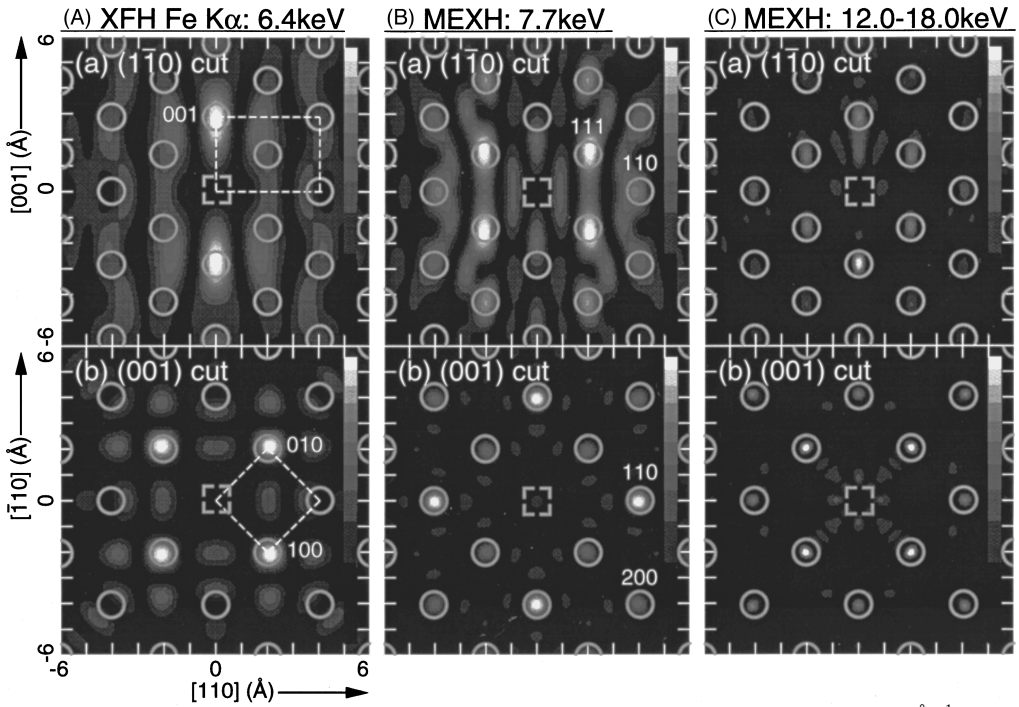

FIG. 2. (A) Theoretically generated atomic images for single-energy XFH with Fe K-α fluorescent radiation ($k=3.245$ Å^{-1} or $E=6.40$ keV), obtained from a model 189-atom Fe(001) bcc cluster. Cross-section cuts are shown for (a) a vertical (110) plane and (b) a horizontal (001) plane. The actual locations of the atoms are indicated as circles. The location of the emitter, which is not imaged, is indicated by the dashed square at the origin. The bcc unit cell is indicated by the dashed lines. (B) As (A), but for single-energy MEXH ($k=3.902$ Å^{-1} or $E=7.70$ keV) images. (C) As (A), but for multiple-energy MEXH (seven energies spanning $k=6.081$ to 9.122 Å^{-1} or $E=12.00$ to 18.00 keV) images. Note the image cancellations for different atoms in (A) and (B), while all near-neighbor atoms surrounding the emitter in (C) are visible.

atoms ($\mathbf{r}=\mathbf{a}_j$).[4] This is a transform over some volume in $\mathbf{k}$ space with a kernel ($e^{-i(\mathbf{k}\cdot\mathbf{r}-kr}$), which produces a stationary phase with the path length difference factor and yields image intensities located at relative positions $\mathbf{r}$ via

$$U(\mathbf{r})=\int_k k^2 dk \int\int_\Omega d\sigma_{\mathbf{k}} e^{-i(\mathbf{k}\cdot\mathbf{r}-kr)}\chi(\mathbf{k}). \qquad (4)$$

If the scattering factor in Eq. (1) is weak and fairly isotropic (as is the case with x rays), then the resulting holographic images will be located very close to the actual atomic positions, and will be much freer from undesirable aberrations and artifacts.[10–12,19] Various modifications to the basic reconstruction transforms of Eqs. (3) and (4),[13,15] as well as entirely different reconstruction algorithms,[16,17] have been proposed to account for the anisotropic emission and scattering processes inherent in electron holography.

The above discussion has emphasized the equivalence of XFH and MEXH due to the optical reciprocity theorem, where the two methods can be thought of as time-reversed cases of each other. However, this symmetry is broken when the manner in which atomic fluorescence is used to measure the path length differences between scattered and unscattered wave fronts is considered. Thus, in XFH the fluorescent x ray of a definite energy is used as the source of the direct and scattered waves, whereas in MEXH the same fluorescent x ray is used as a detector of the exciting x-ray wave field, *which can be at any energy above the fluorescence threshold*. Thus, despite the reciprocal equivalence of XFH and MEXH, as discussed in the previous section above, there are significant differences between them, including the fact that *XFH and MEXH holograms cannot be recorded at the same energy*.

III. Theoretical holographic images for Fe bcc. This section discusses theoretical images for XFH and MEXH, derived for choices of photon energies that would be accessible and/or selected for optimum image formation in experiments on a real system (bcc Fe).

In XFH, because a fluorescing atom is used as the wave source, one may only record holograms at the characteristic fluorescent energies of the emitting atom species. Figure 2(A) show the expected atomic images reconstructed via Eq. (3) from a theoretical XFH $\chi(\mathbf{k})$ calculated for Fe $K\alpha$ emission ($k=3.245$ Å^{-1} or $E=6.40$ keV). This hologram was calculated on a $5°\times5°$ grid in polar and azimuthal angles from a model 189-atom Fe(001) bcc cluster, using a single scattering model that includes the full complex atomic scattering factor for x rays.[19,23] Some of the Fe atoms in these images are clearly imaged, but they are only modestly resolved, a major reason being the long wavelength of the x rays at this energy ($\lambda=1.937$ Å). While higher Z atoms in general have more energetic fluorescence energies, and thus could produce higher resolution atomic images, reconstructions from XFH holograms from low Z emitters will be much less practical. Of note here is that of the neighboring sites immediately surrounding the emitter, only the 001 and 100 atom (and their symmetry-related sites) are visible, while the 200 and 110 atoms are missing [see Fig. 2(B) for the locations of the latter atoms]. This is due to a well-recognized problem with single-energy holography:[18,19] at this 6.40 keV energy the real and twin images of both the 200 and 110 atoms overlap out of phase, suppressing the image intensity at these locations. These real-twin image overlaps are an inherent problem in reconstructing centrosymmetric atomic-structure images from single-energy

holograms, but using more than one energy promises to solve this problem.[19] The 001 and 100 atoms in Fig. 2(A) are also shifted slightly outwards (by ~0.05 Å) from their actual locations due to the angular dependence of the small scattering phase shift at this energy. This is found to be of the form $\psi(\Theta_{\mathbf{a}_j}^{\mathbf{k}}) \propto \beta(1-\cos\Theta_{\mathbf{a}_j}^{\mathbf{k}})+\gamma$, with $\beta \approx 0.09$ and $\gamma \approx 0.19$, which is expected to cause position shifts of $\Delta r \approx \beta/k \approx 0.03$ Å in the reconstructed images.[10]

In MEXH, the unscattered and direct wave fronts are generated by a coherent far-field source, which can be tuned to *any* desirable x-ray energy above an absorption edge (7.11 keV at Fe K), with the fluorescence serving only as a detector for the resulting path length differences between the scattered and direct wave fronts. Figure 2(B) shows the expected Fe atomic images reconstructed via Eq. (3) from a theoretical *single-energy* MEXH hologram at $k=3.902$ Å^{-1} ($E=7.70$ keV, chosen to be just above various near-edge effects), for the same model Fe bcc cluster as in Fig. 2(A). The resolution of the Fe images is slightly improved, due to the slightly shorter wavelength of x rays used ($\lambda=1.610$ Å). But note that the 111 and 110 atoms are now visible, while the 001 and 100 atoms are suppressed due to changes in the real-twin overlap at this choice of hologram energy. The relative brightness in intensity of the 111 atomic image, compared to the 110, 001, and 200 atomic image in Fig. 2(B), indicates that these latter atomic images are almost real-twin image suppressed. The 111 image intensities are also shifted outwards by 0.04 Å, again due to the phase ($\beta \approx 0.12$ and $\gamma \approx 0.19$, making $\Delta r \approx \beta/k \approx 0.03$ Å) of the complex atomic scattering factor at this hologram energy.[10]

Ideally, one could record single-energy holograms at various energies, and simply superpose their reconstructed images in order to override the real-twin image suppression conditions for different centrosymmetric atomic pairs at different energies. However, it is much more advantageous to reconstruct images from a single data set of multiple hologram energies via Eq. (4), such that the holographic data points used in the image reconstruction span a **k**-space volume. This improves the resulting atomic images, as the transform of Eq. (4) breaks the symmetry between the real and twin terms in Eq. (2) when extended over a finite energy (or k) range.[4,19] The use of multiple-energy holograms in reconstructing atomic images is in fact commonplace in electron emission holography (e.g., due to the tunability of the photoelectron energy of the source atom), where it has been shown to suppress the presence of undesirable twin images, and to increase image fidelity.[5–9,14–17]

Figure 2(C) now shows the expected Fe atomic images reconstructed from a theoretical seven-energy MEXH data set, spanning $k=6.081$ to 9.122 Å^{-1} ($E=12.00$ to 18.00 keV), with $\delta k=0.507$ Å^{-1} (corresponding to an energy interval of $\delta E=1.00$ keV), for the same model Fe bcc cluster as in Figs. 2(A) and 2(B). These atomic images are better resolved than Figs. 2(A) and 2(B), due to the shorter-range x-ray wavelengths used ($\lambda=1.033$ to 0.689 Å), and are more resolved than any single-energy holographic image within this range of energies.[4] *All* near-neighboring atoms surrounding the emitter are furthermore clearly imaged with no real-twin cancellations present. The presence of faint aberrations and artifacts visible in the single-energy holographic of Figs. 2(A) and 2(B) have also been further suppressed. In XFH it would be possible in principle to measure holograms at the different fluorescence energies of a specific emitter type in order to suppress real-twin image overlaps. However, the limited number and varying intensities and spacings of these characteristic energies would present severe constraints on the reconstruction of multiple-energy holograms in XFH.[19]

IV. Conclusions. The evolution of Gabor in-line holography into XFH and MEXH has been discussed, as well as the equivalence of XFH and MEXH for single-energy holograms by virtue of the optical reciprocity theorem. However, XFH and MEXH holograms cannot be recorded at the same energy. XFH data can only be recorded at the characteristic fluorescence energies of an emitting atom, and thus XFH images may suffer from the unavoidable effects of real and twin images overlapping (including out of phase overlap, producing image cancellations), as well as undesirable aberrations and artifacts inherent in single-energy holographic images. In XFH, however, a whole single-energy hologram can in principle be instantaneously imaged by a large parallel detector array. This can be advantageous if time-resolved XFH using x-ray laser excitation sources will be attempted. MEXH data can be recorded at any energy *above* the absorption edge of an emitter. Thus, single-energy MEXH data can be taken at those energies where real and twin images will interfere in phase at atomic locations of interest (cf. Fig. 3). More importantly, multiple-energy MEXH data sets can be used to suppress real-twin image overlaps, and thus generate atomic images with better resolution and higher fidelity than any single-energy hologram within the same energy range [cf. Fig. 2(C)].

Research at the University of California, Davis, and the Lawrence Berkeley National Laboratory was supported in part by the Office of Naval Research (Contract Nos. N00014-90-5-1457 and N00014-94-1-0162), by the Director, Office of Energy Research, Office of Basic Energy Sciences, Material Sciences Division of the U.S. Department of Energy (Contract No. DE-AC03-76SF00098), the National Energy Research Supercomputer Center, and by the International Center for Diffraction Data. Research at Oak Ridge National Laboratory beamline X-14 at the National Synchrotron Light Source, Brookhaven National Laboratory, was supported by the Division of Material Sciences and Division of Chemical Sciences of the U.S. Department of Energy, and by Lockheed Martin Energy Systems, Inc. (Contract No. DE-AC05-840R21400).

[1] D. Gabor, Nature (London) **161**, 777 (1948).

[2] H. Schmit *et al.*, J. Vac. Sci. Technol. B **13**, 2428 (1995), and references therein.

[3] A. Szöke, in *Short Wavelength Coherent Radiation: Generation and Applications*, edited by T. Attwood and J. Boker, AIP Conf. Proc. No. 147 (AIP, New York, 1986), p. 361.

[4] J. J. Barton, Phys. Rev. Lett. **61**, 1356 (1988); **67**, 3106 (1991); S. Y. Tong *et al.*, Phys. Rev. B **46**, 2452 (1992), and references therein.

[5] B. L. Petersen *et al.*, Chem. Phys. Lett. **220**, 46 (1994), and references therein; H. Wu *et al.*, Phys. Rev. Lett. **71**, 251 (1993), and references therein; M. Zharnikov *et al.*, Surf. Sci. **334**, 114 (1995), and references therein; R. Denecke *et al.*, *ibid.* **331-333**, 1085 (1995); J. G. Tobin *et al.*, *ibid.* **334**, 263 (1995), and references therein.

[6] H. Li *et al.*, Phys. Rev. B **47**, 10 036 (1993); D. K. Saldin *et al.*, *ibid.* **48**, 8234 (1993), and references therein.

[7] Z.-L. Han *et al.*, Surf. Sci. **258**, 313 (1991), and references therein; I. H.

Hong *et al.*, Phys. Rev. B **52**, 16 884 (1995), and references therein.
[8] M. A. Mendez *et al.*, Phys. Rev. B **45**, 9402 (1992), and references therein; C. M. Wei *et al.*, Phys. Rev. Lett. **72**, 2434 (1994), and references therein.
[9] S. Y. Tong *et al.*, Phys. Rev. Lett. **69**, 3654 (1992).
[10] D. K. Saldin *et al.*, Phys. Rev. B **44**, 2480 (1991).
[11] S. Thevuthasan *et al.*, J. Vac. Sci. Technol. A **10**, 2261 (1992).
[12] P. Hu and D. A. King, Phys. Rev. B **46**, 13 615 (1992).
[13] B. P. Tonner *et al.*, Phys. Rev. B **43**, 14 423 (1991).
[14] S. Y. Tong *et al.*, Phys. Rev. B **51**, 1850 (1995); H. Wu and G. J. Lapeyre, *ibid.* **51**, 14 549 (1995); J. M. Roesler *et al.*, Surf. Sci. **329**, L588 (1995), and references therein.
[15] P. J. Rous and M. H. Rubin, Surf. Sci. **316**, L1068 (1994).
[16] P. Hofmann *et al.*, J. Vac. Sci. Technol. A **12**, 2045 (1994); Surf. Sci. **337**, 169 (1995), and references therein.
[17] X. Chen and D. K. Saldin, Phys. Rev. B **50**, 17 463 (1994).
[18] M. Tegze and G. Faigel, Europhys. Lett. **16**, 41 (1991).
[19] P. M. Len *et al.*, Phys. Rev. B **50**, 11 275 (1994).
[20] M. Tegze and G. Faigel, Nature (London) **380**, 49 (1996).
[21] T. Gog *et al.*, Phys. Rev. Lett. **76**, 3132 (1996).
[22] T. Gog *et al.*, Synch. Rad. News **9**, 30 (1996).
[23] *International Tables for X-ray Crystallgraphy*, edited by K. Lonsdale (Reidel, Dordrecht, 1968), Vol. III.